Hindawi
Journal of Nanomaterials
Volume 2018, Article ID 9890785, 14 pages
https://doi.org/10.1155/2018/9890785

Research Article

Evolution Mechanism of Metallic Dioxide MO_2 (M = Mn, Ti) from Nanorods to Bulk Crystal: First-Principles Research

Pengsen Zhao,[1] Guifa Li,[1] Bingtian Li,[1] Haizhong Zheng,[1] Shiqiang Lu,[1] and Ping Peng[2]

[1]*Key Laboratory of Jiangxi Province for Persistent Pollutants Control and Resources Recycle, Nanchang Hangkong University, Jiangxi 330063, China*
[2]*School of Material Science and Engineering, Hunan University, Hunan 410082, China*

Correspondence should be addressed to Guifa Li; lgf_918@126.com

Received 23 November 2017; Accepted 4 March 2018; Published 4 April 2018

Academic Editor: Nageh K. Allam

Using first-principle calculations, the surface energy, cohesive energy, and electronic properties of α-MnO_2 and rutile TiO_2 nanorods and microfacets were investigated and clarified to, in the first instance, determine the evolution mechanism. The results show that the surface energies of α-MnO_2 nanorods and microfacets conform to function $1.0401\,Jm^{-2} + N \times 0.608\,Jm^{-2}$, while the surface energies of the rutile TiO_2 nanorods and microfacets are governed by a 1.0102×1.1997 rule. Their electronic properties, such as the Mulliken population and Mulliken charge, can only be normalized by their surface areas to attain a linear function. Meanwhile, the surface energy of α-MnO_2 with the nanostructure closely conforms to the function for normalized Mulliken population and Mulliken charge as $f(x) = 102.9 \times x + 0.101$ with an R^2 value of 0.995. Thus, our research into the evolution mechanism affecting the surface effect of nanometer materials will be useful for investigating the intrinsic mechanism of the nanometer effect and doping process of metallic dioxide catalysts.

1. Introduction

TiO_2, which is a vital inorganic functional nanomaterial, has been widely used in down-flop pigments, ultraviolet screening, photoelectric conversion, photocatalysis, and so on [1]. MnO_2 is a popular and cost-effective material for the removal of pollutants in air, water, and industry [2]. Both have been widely investigated and improved to enhance their catalytic performance, such as by doping with metallic elements [1, 3], incorporation into carbon nanotubes [4], and manufacturing with a nanometer structure [5]. Especially, in the nanocrystallization process, the TiO_2 and MnO_2 nanometer materials exhibit additional surface and nanometer effects although they have the same components and skeleton units as the bulk morphology. Both have been successfully applied to catalytic redox for some pollutants. But they exhibit different catalytic capabilities for the same reactant in somewhere. To remove arsenite oxidation, the arsenite (As^{III}) is oxidized to As^{V} for more than 0.4 hours by manganese dioxide, and the Mn-As bond length is from 0.271 nm to 0.34 nm [6]. For the rutile TiO_2, however, it is found that the Ti-As bond length is from 0.283 nm to 0.405 nm, and the adsorption energy of As^{V} on TiO_2(110) is greater than that on MnO_2 [7]. Regarding the decomposition of CO, Chen et al. [8] indicated that the CO adsorbed onto the anatase TiO_2 resulted in a moderate adsorption energy (about 0.3 eV) and a positive shift of the C-O stretching frequency (about $+44\,cm^{-1}$) whereas the CO could no longer be adsorbed onto the MnO_2 [9]. Considering the adsorption of O_2 onto MnO_2, the oxygen reduction reaction can occur either in solution [10] or in air [11]. Meanwhile, Petrik and Kimmel [12] stated that O_2 could be adsorbed onto rutile TiO_2 only at very low temperatures. Their different catalytic activities have attracted the attention of many researchers. Barnard et al. [13] had modeled the electronic properties of TiO_2 nanoparticles and pointed out that the free energy of surface would keep constant after the sizes of nanoparticles were larger than 100 nm [14]. After studying a series of low stoichiometric surfaces, they found the effects of edges and corners were omitted when the nanoparticles were larger than ~2 nm, and constructed the morphology of rutile TiO_2 only composed by {110} Miller index [15]. Nevertheless, Deringer and Csányi

[16] and Tompsett et al. [17] discovered that nanorods of rutile TiO_2 and α-MnO_2 have the same equilibrium geometric morphologies, with a structure consisting mainly of {100} and {110} Miller indexes. Furthermore Hummer et al. [18] pointed out that the surface energies of TiO_2 were dependent with edges and corners of nanocrystal at particle size ≤3 nm. At present, former researches do not identify the intrinsic mechanism between bulk and nanorods although they have studied the nanoscale morphology of rutile TiO_2 and α-MnO_2 for a long time. But such an intrinsic mechanism plays a vital role in the design and optimization of metallic oxide nanomaterials. In a previous paper [19], it have been stated that there may be an optimal α-MnO_2 nanorod, which has a surface energy suitable for promoting enhanced surface activity, together with an appropriate degree of cohesive energy for maintaining structural stability. As an extension of previous work, the present study further sets out to investigate the evolution mechanism of bulk and nanorods of MO_2 (M = Mn, Ti) metallic dioxide.

2. Simulation Models and Method

To elucidate the nanometer effect of metallic dioxide MO_2 (M = Mn, Ti) with a nanostructure, several models of MO_2 (M = Mn, Ti) in crystal, bulk surface, nanorod, and microfacet topological configurations were constructed and studied systematically according to their stoichiometric proportions. Their corresponding simulated models are shown in Figures 1 and 2. Regarding the rutile TiO_2 model construction, only two prominent and stable Miller index planes, such as {100} and {110}, are considered. In the present study, the α-MnO_2 and rutile TiO_2 nanorod models were constructed based on the experimental results obtained by Barnard et al. [13–15] and Deringer and Csányi [16]. All the simulation models are shown in Figure 2. For the rutile TiO_2 (100) bulk surface, there are triple units of {100} Miller index slabs, while, for the {110} bulk surfaces, there are double {110} Miller index slabs, as shown in Figures 2(b) and 2(c), respectively. A microfacet rutile TiO_2 [(100 × 110)] supercell structure containing only double units of {100} and {110} Miller index slabs, which had been proven to exhibit a similar catalysis performance as a nanostructure [19, 22], was built as a bulk surface with nanometer morphologies only, as shown in Figure 2(d). Regarding the nanorod (NR) models, all of them were combined with only {110} and {100} Miller index slabs, as shown in Figures 2(e)–2(g). (In our future work, further Miller index slabs will be considered to represent a more complicated situation.) The smallest nanorod addressed in the present study, that is, (NR(1)), consisting of two {110} and one {100} Miller index slab unit, was built as a $Ti_{32}O_{64}$ supercell, as shown in Figure 2(e). The second rutile TiO_2 nanorod (NR(2)) contains two units each of {100} and {110} Miller index slabs to construct a $Ti_{52}O_{104}$ supercell (Figure 2(f)). The largest rutile TiO_2 nanorod contains triple {110} and double {100} Miller index slab units named NR(3), which form a $Ti_{88}O_{176}$ supercell (Figure 2(g)). Similar way of constructed configuration is forced to α-MnO_2 nanorods. The latter is the largest that can be handled in the calculation limits of our computer cluster. All these primitive nanorods can be regarded as being free nanomaterials in morphologies by using their periodic boundary conditions and transitional symmetry. The purpose of such constructions is to investigate the surface effect of different Miller indices over several models. All the bulk surface models were calculated assuming slabs with a minimum thickness of 14 Å. In all the bulk surface and nanorod models, a separating vacuum distance of at least 12 Å was used to distance the slabs from their periodic image. For the first step, all of the models were not terminated by hydrogenation as followed by Barnard et al.'s report [13]. The complicated surface models of metallic dioxide MO_2 (M = Mn, Ti) will be studied in our further research. To distinguish the difference between α-MnO_2 and rutile TiO_2 in similar configurations, every simulated model was labeled "M" or "T" to represent the α-MnO_2 and rutile TiO_2 series, respectively. For example, the (100) bulk surface for α-MnO_2 was labeled M(100), while T(100) represents the (100) bulk surface for rutile TiO_2. This convention is used for every model shown in Figures 1 and 2.

Based on the calculated sets of Deringer and Csányi [16], all the above α-MnO_2 and rutile TiO_2 simulation models were relaxed by applying the following process: a first-principles pseudopotential plane-wave method, based on density functional theory, was implemented in the Cambridge Sequential Total Energy Package (CASTEP) code [23]. The electronic structure was calculated using the Generalized Gradient Approximation (GGA) devised by Perdew et al., with a Tkatchenko-Scheffler approach (TS) being used for the dispersion corrections [16]. The PBE + U exchange-correlation function has been demonstrated to give a good description of the defect properties in α-MnO_2 [17]. All calculations were performed in a ferromagnetic spin polarized configuration, while effects of more complex magnetic orders were left for future work due to their low energy scale. For the rutile TiO_2, however, Deringer and Csányi [16] pointed out that adding U terms caused the results to steadily be worsened, in much the same way as in [22, 24]. In the present study, therefore, U correction was not applied to any of the rutile TiO_2 models. All the subsequent calculations were performed based on the equilibrium lattice constants obtained without cell relaxation using a cutoff of 500 eV, which was more precise than previous papers [13–15, 18]. This included the recalculation of the energy for the bulk unit cell so that all the comparative energies could be obtained. A minimum of 8 × 1 × 1 k-points were used in the Brillouin zone of the conventional cell and scaled appropriately for supercells. All the atomic positions in these primitive cells were relaxed in spin polarized situation according to the total energy and force using the Broyden–Fletcher–Goldfarb–Shanno (BFGS) algorithm scheme [25], based on the cell optimization criteria (a root mean square (RMS) force of 0.03 eV/Å, a stress of 0.05 GPa, and a displacement of 0.001 Å). The convergence criteria for the self-consistent field (SCF) and energy tolerances were set to 1.0×10^{-6} and 5.0×10^{-5} eV/atom, respectively.

3. Results and Discussion

3.1. Test of Potential. The value of the U parameter for our PBE + U calculations is determined by ab initio calculations.

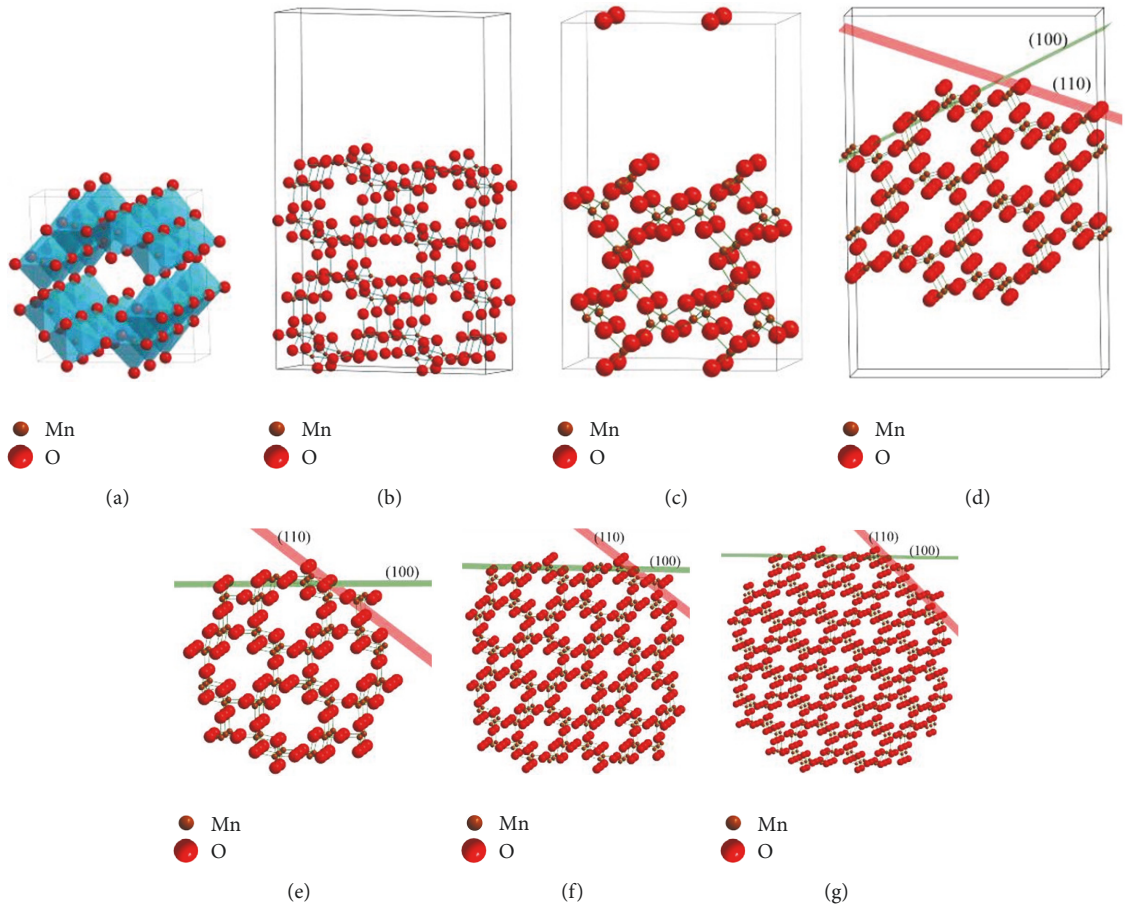

Figure 1: Simulated several morphologies of Hollandite MnO_2 models, where (a) α-MnO_2 crystal (Mn_8O_{16}), (b) (100) bulk surface ($Mn_{32}O_{64}$, M(100)), (c) (110) bulk surface ($Mn_{16}O_{32}$, M(110)), (d) [(100 × 110)] microfacet ($Mn_{32}O_{64}$, M[(100 × 110)]), (e) nanorod(I) ($Mn_{28}O_{56}$, MNR(I)), (f) nanorod(II) ($Mn_{68}O_{136}$, MNR(II)), and (g) nanorod(III) ($Mn_{112}O_{224}$, MNR(III)).

Table 1: Predicted PBE + U, experimental and theoretical lattice parameters for α-MnO_2.

TiO_2	a (Å)	b (Å)	c (Å)
This work	9.922	9.922	2.904
Ref. [17]	9.907	9.907	2.927
Exp. [20]	9.750	9.750	2.861

Table 2: Predicted DFT + TS, experimental and theoretical lattice parameters for rutile TiO_2.

TiO_2	a (Å)	b (Å)	c (Å)
This work	4.62	4.62	2.95
Ref. [16]	4.61	4.61	2.97
Exp. [21]	4.58	4.58	2.95

Previous study [10] has demonstrated that a good description of the structural stability, band gaps, and magnetic interactions can be obtained when PBE + U is applied with the fully localized limit, which is therefore also used in the present study. U = 2.0 eV is employed for α-MnO_2. Table 1 lists the calculated lattice parameters for α-MnO_2 obtained from PBE + U. These results are within 1.8% of the theoretical [17] and experimental [20] parameters, but the common tendency for PBE + U to overestimate the unit cell volume is evident. Regarding the values listed for rutile TiO_2 in Table 2, the results are also similar to those of theoretical [16] and experimental [21] reports on DFT + TS. Therefore the calculated sets are appropriate for investigating the surface effects of MO_2 (M = Mn, Ti).

3.2. Evolution Character of Surface Energy. In Tables 3 and 4, the surface energy $E_{surface}$ for α-MnO_2 and rutile TiO_2 obtained via PBE + U and DFT + TS calculations, respectively, is shown. The surface energy is calculated by taking the difference between the energy of a constructed slab and the same number of α-MnO_2 or rutile TiO_2 formula units in the bulk [19]:

$$E_{surface} = \frac{E_{total} - nE_b}{S}, \quad (1)$$

where E_{total} is the energy of a surface or nanorod model containing n formula crystal units, E_b is the total energy of the crystal, and S is the surface area of the simulated models, where the bulk surface and microfacet contain two surfaces

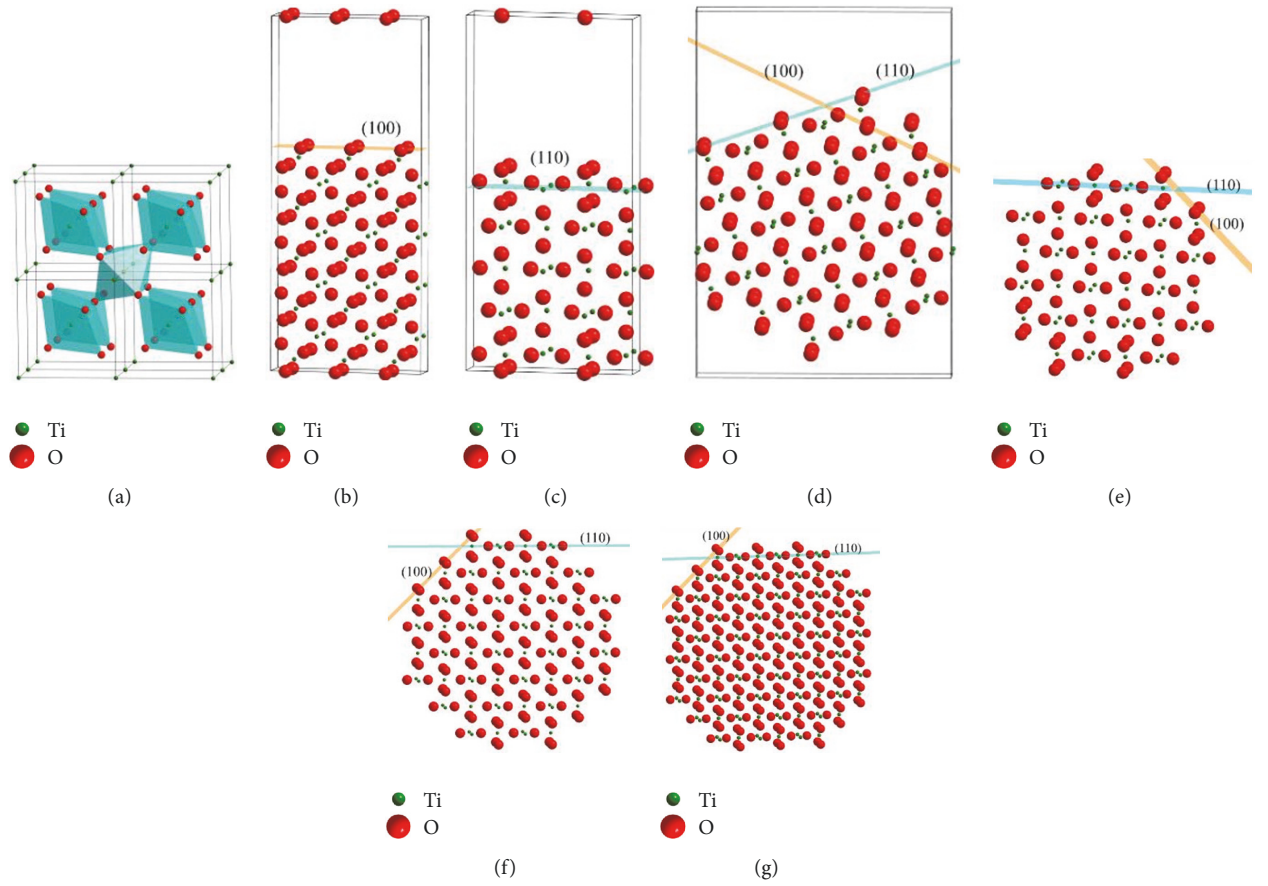

FIGURE 2: Simulated several morphologies of rutile TiO_2 models, where (a) TiO_2 crystal supercell ($Ti_{16}O_{32}$), (b) (100) bulk surface ($Ti_{27}O_{54}$, T(100)), (c) (110) bulk surface ($Ti_{20}O_{40}$, T(110)), (d) [(100 × 110)] microfacet ($Ti_{34}O_{68}$, T[(100 × 110)]), (e) nanorod(1) ($Ti_{32}O_{64}$, TNR(1)), (f) nanorod(2) ($Ti_{52}O_{104}$, TNR(2)), and (g) nanorod(3) ($Ti_{88}O_{176}$, TNR(3)).

by their periodic boundary condition. The results are shown in Figure 3 (as well as in Tables 3 and 4). In [19], it is shown that the $E_{surface}$ values of the α-MnO_2(100) and (110) bulk surfaces are equal to 0.6503 Jm^{-2} and 0.6794 Jm^{-2}, respectively, which are similar to the results reported by Tompsett et al. (0.64 Jm^{-2} and 0.75 Jm^{-2}, resp.) [17]. Regarding the rutile TiO_2, the $E_{surface}$ value for the T(100) is equal to 1.2492 Jm^{-2}, which is a little larger than that (1.00 Jm^{-2}) obtained by Deringer and Csányi [16]. Furthermore, the $E_{surface}$ value of the T(110) is equal to 1.1503 Jm^{-2}, which is similar to that (1.10 Jm^{-2}) obtained by Ramamoorthy et al. [26], but a little larger than the 0.81 Jm^{-2} obtained by Lindan et al. [27] and the 0.80 Jm^{-2} obtained by Deringer and Csányi [16]. However, none of them influence the trend and the internal law governing the surface energy in this manuscript.

The results are shown in Figures 3 and 4. For α-MnO_2, it is found that the $E_{surface}$ value increases according to a trend of $E_{surface}$M(100) < $E_{surface}$M(110) < $E_{surface}$MNR(I) < $E_{surface}$MNR(II) < $E_{surface}$MNR(III) < $E_{surface}$M[(100 × 110)], as shown in Figure 3(a) (labeled by ①). Given that the surface energies of M(100) and M(110) are nearly equivalent, the abscissa has no physical significance. Therefore, it assumes that the abscissa value of M(100) and M(110) is 2.5 and that of M[(100 × 110)] is 9, which is greater than that of MNR(III) by 3 points, as shown in Figure 3(a) (labeled by ②). It is found that the surface energies of α-MnO_2 of different morphologies fall in line with the relationship among them, implying the existence of an internal correlation. Furthermore, the sequence of M[(100 × 110)] does not correspond to nanorod(III), because other nanorods may exist. Upon closely analyzing their geometric structure, it is found that all the α-MnO_2 nanorods and microfacets are composed of two Miller indexes, for example, the (110) and (100) microsurfaces. They differ only in the numbers of the (110) and (100) microsurfaces. If it is hypothesized that the average of the values of $E_{surface}$M(100) and $E_{surface}$M(110) is one component element of the surface energy for the nanorods and microfacets, their surface energies exhibit some linear relationship. This has not been observed previously. Their formulized relationship can be explained as follows: one constant parameter of the surface energy, 1.0401 Jm^{-2}, labeled A, and another constant parameter of the surface energy, 0.6648 Jm^{-2} labeled B, which is equal to the average of $E_{surface}$M(100) and $E_{surface}$M(110), that is, (0.6593 Jm^{-2} + 0.6974 Jm^{-2})/2 = 0.6648 Jm^{-2}. The correlation function for the surface energy of the nanorods and microfacets to the average value of the surface energy

Table 3: Surface energy ($E_{surface}$) and cohesive energy ($E_{cohesive}$) of α-MnO_2 crystal, bulk surface, and nanorod models.

	Models	E_{total} (eV)	A (Å)	B (Å)	S (Å^2)	$E_{surface}$ (eV)	$E_{surface}$ (Jm^{-2})	$E_{cohesive}$ (eV)
Crystal	Mn_8O_{16}	−11734.8960	—	—	—	—	—	−4.7223
Bulk surface	M(100)	−46934.8997	2.9040	19.8440	57.6265	4.6843	0.6503	−4.6735
	M(110)	−23466.2580	2.9040	14.3292	41.6116	3.5340	0.6794	−4.6487
Microfacet	M[(100 × 110)]	−11734.8960	2.9040	24.2512	70.4255	44.4003	5.0437	−4.2598
Nanorod	MNR(I)	−41029.8368	2.9040	68.3480	198.4811	42.2991	1.7040	−4.2188
	MNR(II)	−99651.0223	2.9040	108.0360	313.7342	95.5937	2.4376	−4.2537
	MNR(III)	−164137.7267	2.9040	137.0160	397.8914	150.8172	3.0323	−4.2735

Table 4: Surface energy ($E_{surface}$) and cohesive energy ($E_{cohesive}$) of rutile TiO_2 crystal, bulk surface, and nanorod models.

	Models	E_{total} (eV)	a (Å)	B (Å)	S (Å^2)	$E_{surface}$ (eV)	$E_{surface}$ (Jm^{-2})	$E_{cohesive}$ (eV)
Crystal	Ti_2O_4	−2481.8319	—	—	—	—	—	−7.8669
Bulk surface	T(100)	−67003.1105	2.9528	13.7748	81.3473	6.3510	1.2492	−7.7885
	T(110)	−49631.1245	2.9528	12.9870	76.6949	5.5137	1.1503	−7.7750
Microfacet	T[(100 × 110)]	−84372.5298	2.9528	44.6000	131.6929	9.7551	1.1852	−7.7712
Nanorod	TNR(1)	−79405.0467	2.9528	60.6920	179.2087	13.5744	1.2119	−7.7255
	TNR(2)	−129037.4570	2.9528	77.9360	230.1260	17.8022	1.2377	−7.7528
	TNR(3)	−218377.7220	2.9528	102.5320	302.7520	23.4859	1.2412	−7.7779

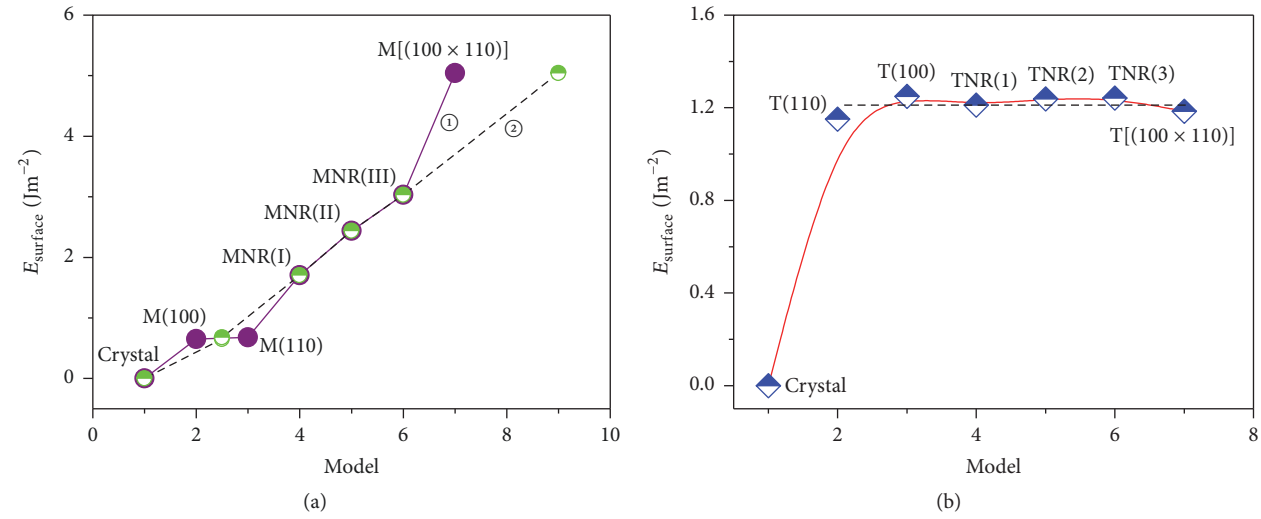

FIGURE 3: Surface energy of α-MnO_2 and rutile TiO_2 in different morphologies.

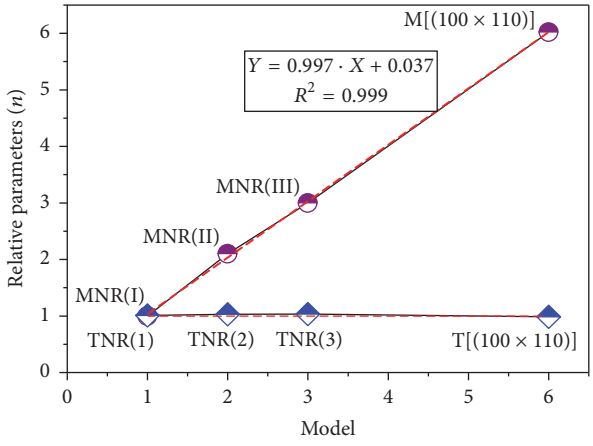

FIGURE 4: Formulized treatment on surface energy of α-MnO_2 and rutile TiO_2 in different morphologies.

for M(100) and M(110) is given as $Y = A + N \times B$, where N is the quantization parameter for different nanorods and microfacet models. Quantization parameter N plays two roles in this paper: firstly it implies that their surface energies have some relationship between nanorods and corresponding bulk surface; secondly it restricts the maximum value of surface energy for nanorods. And N is defined as the additional number of {110} or {100} Miller index slab units from minimum nanorod MR(I) or NR(I), wherein the quantization parameter N for MNR(I) or TNR(I) is equal to 1, respectively. Their quantization parameter N is shown Figure 4. Their N values closely follow a linear relationship. After fitting by linear regression, the adjusted R square (R^2) value is equal to 0.999, as shown in Figure 4. We can thus derive a function for the surface energy: $E_{surface}$MNR(I) = 1.0401 Jm^{-2} + 1 × 0.6648 Jm^{-2}, $E_{surface}$MNR(II) = 1.0401 Jm^{-2} + 2.1021 × 0.6648 Jm^{-2}, $E_{surface}$MNR(III) = 1.0401 Jm^{-2} + 2.9967 × 0.6648 Jm^{-2}, and $E_{surface}$M[(100 × 110)] = 1.0401 Jm^{-2} + 6.0226 × 0.608 Jm^{-2}. Thus, it is clear why a previous adjustment of the abscissa in the surface energy of α-MnO_2 was a line correlation (Figure 3(a) labeled by ②). This reveals the evolution character of the surface energy for α-MnO_2 nanorods and microfacets.

It is well known that the geometrical and chemical performances of rutile TiO_2 are similar to those of α-MnO_2. From the results of analysis, the surface energy of α-MnO_2 nanorods and microfacets has a quantization character. Therefore, it is needed to determine whether there is the same for rutile TiO_2. To do so, the surface energies of the rutile TiO_2 are shown in Figure 3(b) and in Table 4. The trend in the surface energy $E_{surface}$ for rutile TiO_2 from bulk surface → nanorod → microfacet was found to be different from that of α-MnO_2. Their surface energies were found to be similar to each other. The difference between them is very small, as shown in Figure 3(b). For example, the largest $E_{surface}$ is for T(100), which is equal to 1.2492 Jm^{-2}. The smallest is for T(110), which is equal to 1.1503 Jm^{-2}. Their difference is only 0.0989 Jm^{-2}. Furthermore, the differences between the microfacet and nanorods are obviously very small. Therefore, the trend in the surface energy for the rutile TiO_2 in a bulk surface and nanorods assumes a horizontal line, as shown in Figure 3(b). In deep analysis, the microfacet and nanorod models are also composed of two Miller indexes, for example, (110) and (100) microsurfaces. And it takes the average of $E_{surface}$T(100) (1.2492 Jm^{-2}) and $E_{surface}$T(110) (1.1503 Jm^{-2}) as one constant B', where B' is equal to (1.2492 Jm^{-2} + 1.1503 Jm^{-2})/2 = 1.1997 Jm^{-2}. It is found that the relationship between the surface energy of microfacets/nanorods and constant B' can also be fitted by linear regression, as shown in Figure 4. The surface energy function is given by $E_{surface}$TNR(1) = 1.0102 × 1.1997 Jm^{-2}, $E_{surface}$TNR(2) = 1.0317 × 1.1997 Jm^{-2}, $E_{surface}$TNR(3) = 1.0347 × 1.1997 Jm^{-2}, and $E_{surface}$T[(100 × 110)] = 0.9879 × 1.1997 Jm^{-2}. This evolution character of the surface energy of rutile TiO_2 is different from that for α-MnO_2. The quantization character

for α-MnO_2 nanorods is a positive integer, while that for rutile TiO_2 is equal to 1. However, they all have a quantization phenomenon in their surface energies.

3.3. Evolution Character of Cohesive Energy. The cohesive energy represents the work that is required for a crystal to be decomposed into atoms, which in turn denotes the stability of the respective simulation model. Here, the E_{cohesive} value for several α-MnO_2 or rutile TiO_2 models has been calculated from the following equation [19]:

$$E_{\text{cohesive}} = \frac{1}{l+m}\left(E_{\text{total}}^{M_lO_m} - lE_{\text{gas}}^{M} - mE_{\text{gas}}^{O}\right), \quad (2)$$

where l and m represent the number of M (M = Ti or Mn) and O atoms in the respective morphologies of rutile TiO_2 or α-MnO_2, $E_{\text{total}}^{M_lO_m}$ denotes the total energy of the M_lO_m models, and E_{gas}^{M} and E_{gas}^{O} are the energies of the gaseous M (M = Ti or Mn) and O atoms, respectively. Before optimizing the gaseous atoms, a $10 \times 10 \times 10$ (Å^3) vacuum box is constructed and a single atom is placed, such as Ti, Mn, or O, in the center of the box to be relaxed and thus to obtain its global minimum energy. The results are given as $E_{\text{gas}}^{Mn} = -588.1855$ eV and $E_{\text{gas}}^{O} = -432.2548$ eV, as given in Table 3. For rutile TiO_2, the results are $E_{\text{gas}}^{Ti} = -1594.3577$ eV and $E_{\text{gas}}^{O} = -431.9368$ eV, wherein the difference of energy for oxygen in α-MnO_2 and rutile TiO_2 was originated from their different calculated sets in previous part of Simulation Models and Method. The results are given in Table 4. A previous study [19] has discussed the evolution of cohesive energy for α-MnO_2 and found that the structural stability of the nanorods and microfacet is lower than that of the crystal and bulk surfaces. The present study will examine the relationship between the bulk surface, nanorods, and microfacet. If only the absolute values of the cohesive energy are considered, it can only determine that the structural stability of nanorods and microfacet is lower than that of bulk surfaces and crystals, as is already known. Analyzing their geometric morphologies, it is found that they are also composed by two Miller indexes, for example, the (110) and (100) microsurfaces. This paper applies the same treatment to the average value of cohesive energy $E_{\text{a-cohesive}}$ for M(110) and M(100) to establish a basic standard, which is equal to −4.6611 eV/atom (where E_{cohesive}M(110) = −4.6487 eV/atom and E_{cohesive}M(100) = −4.6735 eV/atom) in Figure 5. Considering the ratio n' of the cohesive energy for microfacets and nanorods to $E_{\text{a-cohesive}}$, it is found that every instance of n is nearly equal to 1.09, where $n'_1 = E_{\text{a-cohesive}}/E_{\text{cohesive}}$ MNR(I) = 1.1048, $n'_2 = E_{\text{a-cohesive}}/E_{\text{cohesive}}$ MNR(II) = 1.0958, $n'_3 = E_{\text{a-cohesive}}/E_{\text{cohesive}}$ MNR(III) = 1.0907, and $n'_4 = E_{\text{a-cohesive}}/E_{\text{cohesive}}$ M[(100 × 110)] = 1.0942. It is found that all the correlation constants are equal to 1.09, as shown in Figure 6. This trend, which presents as a horizontal line, is different from the trend in the surface energy. Obviously, a quantization phenomenon can be seen. Regarding the cohesive energy of rutile TiO_2, the difference is found to be very small, unlike the case of α-MnO_2. For example, the most stable structure is the rutile TiO_2 crystal, for which the cohesive energy is equal to −7.8669 eV/atom.

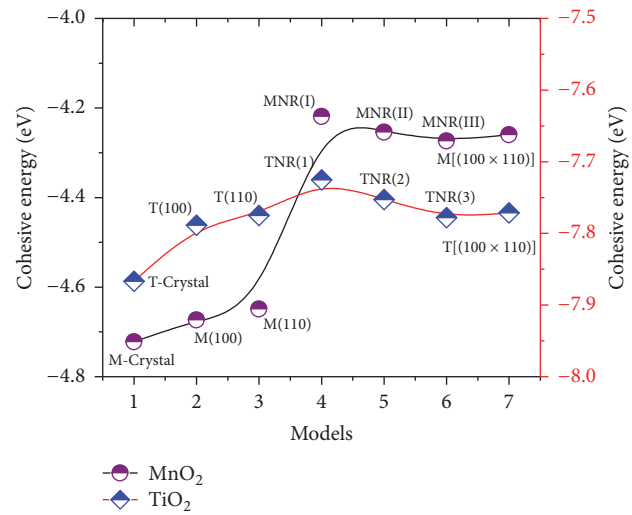

FIGURE 5: Cohesive energy of α-MnO_2 and rutile TiO_2 in different morphologies.

The least stable structure is TNR(1), for which the cohesive energy is equal to −7.7255 eV/atom. The difference between them is only equal to 0.1414 eV/atom. The second stable structure is the bulk surface T(100), for which the cohesive energy is equal to −7.7885 eV/atom. The cohesive energies of the bulk surface T(110), microfacets [(100 × 110)], and TNR(3) are very similar, being −7.7750 eV/atom, −7.7712 eV/atom, and −7.7779 eV/atom, respectively. The difference in their cohesive energies is only 0.0067 eV/atom, which may be regarded as being the calculation error, so that they can all be regarded as having the same structural stability. Regarding the trend in their cohesive energies, shown in Figure 5, they closely approximate to each other. Applying the same treatment to the cohesive energy of rutile TiO_2, it can also take the average value of cohesive energy $E_{\text{a-cohesive}}$ for T(110) and T(100) to be a basic standard, which is equal to −7.7817 eV/atom (where E_{cohesive}T(110) = −7.7750 eV/atom and E_{cohesive}T(100) = −7.7885 eV/atom). Considering the ratio n'' of the cohesive energy for the nanorods/microfacets to $E_{\text{a-cohesive}}$, it is found that every instance of n is nearly equal to 1.00, where $n''_1 = E_{\text{a-cohesive}}/E_{\text{cohesive}}$TNR(1) = 1.0073, $n''_2 = E_{\text{a-cohesive}}/E_{\text{cohesive}}$TNR(2) = 1.0037, $n''_3 = E_{\text{a-cohesive}}/E_{\text{cohesive}}$ MNR(3) = 1.0049, and $n''_4 = E_{\text{a-cohesive}}/E_{\text{cohesive}}$T[(100 × 110)] = 1.0013. All the normalized parameters are nearly equal to 1.00, as shown in Figure 6. Then, the evolution character of the cohesive energy for α-MnO_2 and rutile TiO_2 is abstracted absolutely. In line with the evolution of the geometric morphologies in the growth of nanorods, the ratio of their cohesive energies divided by $E_{\text{a-cohesive}}$ is found to be nearly equal to 1.

3.4. Evolution Character of Electronic Structure. From the above analysis, it is found that, from the bulk surface to nanorods, and even to microfacet with a nanometer structure, the surface and cohesive energies of α-MnO_2 and rutile TiO_2 exhibit some quantization phenomena. It is well known that the surface and cohesive energies are derived from the

Table 5: Normalizing variance of bond length $\sum(\Delta d)^2/s$, Mulliken population $\sum(\Delta Q_{A\text{-}B})^2/s$, and Mulliken charge $\sum(\Delta Q_A)^2/s$ of α-MnO_2 bulk surface, nanorod, and microfacet models.

Models	S (Å^2)	$\sum(\Delta d)^2$	$\sum(\Delta d)^2/s$	$\sum(\Delta Q_{A\text{-}B})^2$	$\sum(\Delta Q_{A\text{-}B})^2/s$	$\sum(\Delta Q_A)^2$	$\sum(\Delta Q_A)^2/s$
M(100)	57.6265	0.114424	0.001986	3.138325	0.05446	0.2984	0.005178
M(110)	41.6116	0.033487	0.000805	1.508575	0.036254	0.1639	0.003939
MNR(I)	198.4811	0.114594	0.000577	2.611850	0.013159	0.2932	0.001477
MNR(II)	313.7342	0.248664	0.000793	6.574800	0.020957	0.6644	0.002118
MNR(III)	397.8914	0.332759	0.000836	10.75690	0.027035	1.0484	0.002635
M[(100 × 110)]	44.4003	0.095139	0.001351	3.009660	0.042735	0.3248	0.004612

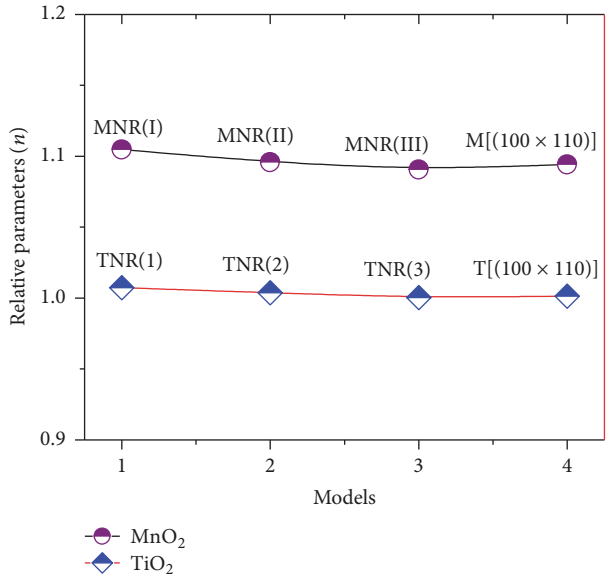

Figure 6: Formulized treatment on cohesive energy of α-MnO_2 and rutile TiO_2 in different morphologies.

geometric or electronic structures. Therefore, in the next section of this paper, we study the evolution of the geometric and electronic structures by applying Mulliken analysis to reveal whether there is any quantization phenomenon corresponding to those energies. The Mulliken population $Q_{A\text{-}B}$ between atoms A and B and the Mulliken charge Q_A are defined as follows [21]:

$$Q_{AB} = \sum_k w_k \sum_\mu^A \sum_\nu^A 2P_{\mu\nu}(k) S_{\nu\mu}(k),$$
$$Q(A) = \sum_k w_k \sum_\mu^A \sum_\nu^A P_{\mu\nu}(k) S_{\nu\mu}(k), \quad (3)$$

where $P_{\mu\nu}$ and $S_{\nu\mu}$ are the density and overlap matrices, respectively, and w_k is the weight associated with the calculated k-points in the Brillouin zone. Usually, the magnitude and sign of Q(A) characterize the ionicity of atom A in the supercell, while $Q_{A\text{-}B}$ can be used to approximate the average covalent bonding strength between atoms A and B. It is known that all the bulk surface, nanorod, and microfacet models originate from their crystal. As a result, the area of the crystal can be regarded as being infinite. To determine the intrinsic mechanism of the evolution character on the surface and cohesive energies, it sets a bond length $d_{A\text{-}B}$, Mulliken population $Q_{A\text{-}B}$, and Mulliken charge Q_A of the crystal as the base values. These base values are equal to the average value of the bond length $\overline{d}_{A\text{-}B}$, the Mulliken population $\overline{Q}_{A\text{-}B}$, and the Mulliken charge $\overline{Q}_A$ in α-MnO_2 or rutile TiO_2 crystal, respectively. Then, the bond length variance $(\Delta d)^2$ is set equal to $(d_{A\text{-}B} - \overline{d}_{A\text{-}B})^2$ to elucidate the influence of the other geometric morphologies, such as the bulk surface, nanorods, and microfacet by their growth. The Mulliken population variance $(\Delta Q_{A\text{-}B})^2$ is equal to $(Q_{A\text{-}B} - \overline{Q}_{A\text{-}B})^2$. However, the Mulliken charge for α-MnO_2 or rutile TiO_2 consists of two parts, namely, the lost charge of metallic elements Mn or Ti and the reception charge of the oxygen elements. Therefore, the Mulliken charge variance $(\Delta Q_A)^2$ is equal to the sum of $(\Delta Q_M)^2$ and $(\Delta Q_O)^2$. In this case, $\overline{d}_{A\text{-}B}$, $\overline{Q}_{A\text{-}B}$, $\overline{Q}_{Mn}$, and $\overline{Q}_O$ for α-MnO_2 are equal to 1.9255, 0.3925, −0.59, and 1.05, respectively. For rutile TiO_2, $\overline{d}_{A\text{-}B}$, $\overline{Q}_{A\text{-}B}$, $\overline{Q}_{Mn}$, and $\overline{Q}_O$ are equal to 1.9714, 0.5050, −0.66, and 1.31, respectively. To identify the quantization phenomenon of the surface effect, the summation of $\sum(\Delta d)^2$, $\sum(\Delta Q_{A\text{-}B})^2$, and $\sum(\Delta Q_A)^2$ by their surface area S is normalized. Although the size and shape of nanocrystal have been set as a function of its free energy [15], the surface area S is the vital factor to affect the chemical performance of nanomaterials. Then the surface area S is chosen to be a normalized parameter in this paper. The detailed data is exhibited in Tables 5 and 6.

The final results are shown in Figure 7. Figure 7 shows that the normalized parameters $\sum(\Delta d)^2/s$, $\sum(\Delta Q_{A\text{-}B})^2/s$, and $\sum(\Delta Q_A)^2/s$ for the bulk surface, nanorod, and microfacet models for α-MnO_2 and rutile TiO_2 fluctuate considerably and exhibit irregularities. Regarding the electronic properties of the bond strength and atomic charge, the largest is for M(100) or T(110) to α-MnO_2 or rutile TiO_2, respectively, as shown in Figures 7(a) and 7(d), whose the surface energy is the smallest for each model. In the case of α-MnO_2, there is an intrinsic law conforming to the configuration evolution, such as the linear correlation between MNR(I) and MNR(III), shown in Figures 7(b) and 7(c). Upon plotting $\sum(\Delta Q_{A\text{-}B})^2/s$ and $\sum(\Delta Q_A)^2/s$ for MNR(I)-MNR(III) and M[(100 × 110)], along with the quantization number N of the abscissa value of 1, 2, 3, and 6, as shown in Figure 8, it is found that they exhibit a linear correlation with R^2 of 0.989 and 0.992, respectively. It is well known that the value of the surface energy sometimes reflects the catalytic performance

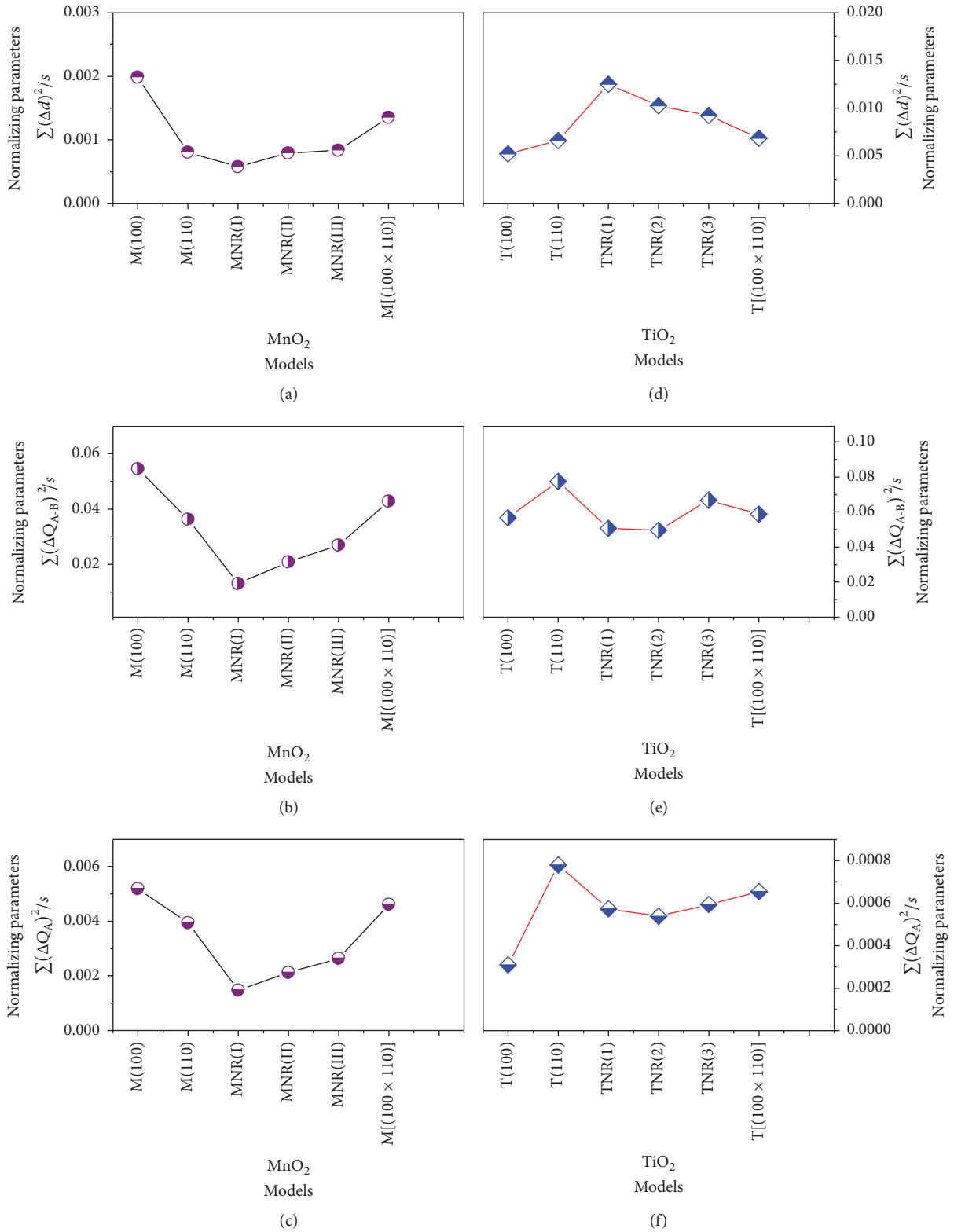

FIGURE 7: Normalizing bond length, Mulliken population, and Mulliken charge of α-MnO_2 and rutile TiO_2 in different morphologies.

Table 6: Normalizing variance of bond length $\sum(\Delta d)^2/s$, Mulliken population $\sum(\Delta Q_{A\text{-}B})^2/s$, and Mulliken charge $\sum(\Delta Q_A)^2/s$ of rutile TiO_2 bulk surface, nanorod, and microfacet models.

Models	S (Å^2)	$\sum(\Delta d)^2$	$\sum(\Delta d)^2/s$	$\sum(\Delta Q_{A\text{-}B})^2$	$\sum(\Delta Q_{A\text{-}B})^2/s$	$\sum(\Delta Q_A)^2$	$\sum(\Delta Q_A)^2/s$
T(100)	81.3473	0.423012	0.0052	4.611500	0.056689	0.0252	0.00031
T(110)	76.6949	0.507518	0.006617	5.946150	0.07753	0.0582	0.000759
TNR(1)	179.2087	1.646453	0.012502	6.671700	0.050661	0.1028	0.000574
TNR(2)	230.1260	2.358380	0.010248	11.433600	0.049684	0.1240	0.000539
TNR(3)	302.7520	2.796938	0.009238	20.220300	0.066788	0.1796	0.000593
T[(100 × 110)]	131.6929	0.899027	0.006827	7.728600	0.058687	0.0837	0.000636

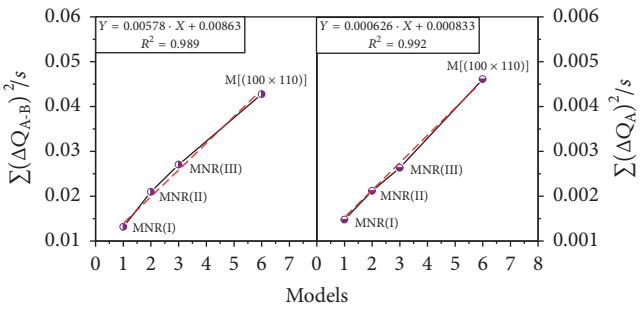

Figure 8: Schematic curve of Normalizing Mulliken population and Mulliken charge of α-MnO_2 in different morphologies with nanostructure.

of materials, in which case the evolution in the normalized Mulliken population and the Mulliken charge of α-MnO_2 nanorods and microfacet are very similar to those of the surface energy, as shown in Figures 3 and 4, thus confirming how the surface catalytic performance of nanomaterials is mainly controlled by the electronic structure. Furthermore, we can assume that the surface energy ($E_{surface}$) is a function of the normalized Mulliken population ($\sum(\Delta Q_{A\text{-}B})^2/s$) and normalized Mulliken charge ($\sum(\Delta Q_A)^2/s$). Their summation ($\sum(\Delta Q_{A\text{-}B})^2/s + \sum(\Delta Q_A)^2/s$) is shown in Figure 9. It noted an absolute linear relationship, as shown in Figures 9(a), 9(b), and 9(c), where the function of $E_{surface}$ versus ($\sum(\Delta Q_{A\text{-}B})^2/s + \sum(\Delta Q_A)^2/s$) is $f(x) = 102.9 \times x + 0.101$ with an R^2 value of 0.995. This indicates that the surface effect in nanomaterials differs from that in bulk materials. Regarding rutile TiO_2, a near-horizontal correlation between TNR(1) and TNR(3) is shown in Figures 7(e) and 7(f). Because all the nanorods and microfacets are composed of {100} and {110} Miller indexes, it can be assumed that their electronic structure originates from that of the (100) and (110) bulk surfaces. These were treated in the same way as their surface and cohesive energies. If we hypothesize that the average value of $\sum(\Delta Q_{A\text{-}B})^2/s$ and $\sum(\Delta Q_A)^2/s$ for M(100) and M(110) is one component element contributing to the evolution character of nanorods and microfacet, their electronic structures can be explored and some linear function can be found. First, we abstracted the average value K of $\sum(\Delta Q_{A\text{-}B})^2/s$ and $\sum(\Delta Q_A)^2/s$ in M(100) and M(110) to be $K_M(Q_{A\text{-}B}) = 0.04535$ and $K_M(Q_A) = 0.004559$, respectively. Second, we abstracted the quantization number by the quotient of the average value of K divided by the corresponding value of $\sum(\Delta Q_{A\text{-}B})^2/s$ and $\sum(\Delta Q_A)^2/s$ for the nanorod and microfacet models. The same treatment was applied to rutile TiO_2, wherein the average value K' of $\sum(\Delta Q_{A\text{-}B})^2/s$ and $\sum(\Delta Q_A)^2/s$ in T(100) and T(110) is found to be $K'_M(Q_{A\text{-}B}) = 0.06711$ and $K'_M(Q_A) = 0.000545$, respectively. The results are shown in Figure 10 and in Tables 5 and 6. Figure 10 shows that there is an obviously linear correlation in the evolution from nanorod to microfacet for α-MnO_2, regardless of the Mulliken population and Mulliken charge. After linear fitting, they obtain a function $f(l) = -0.5921 * l + 4.011$ for $\sum(\Delta Q_{A\text{-}B})^2/s$ and $f(m) = -0.42 * m + 3.461$ for $\sum(\Delta Q_A)^2/s$, respectively, where the quantization number l or m is a positive integer. This evolution law is the same as that of the surface energy shown in Figure 3. For the rutile TiO_2, regardless of the Mulliken population and Mulliken charge, there is another evolution law which is different from that for α-MnO_2. After linear fitting, a near-horizontal line for $\sum(\Delta Q_{A\text{-}B})^2/s$ and $\sum(\Delta Q_A)^2/s$ in the evolution from nanorod to microfacet for rutile TiO_2 is obtained, while the quantization number l or m is close to 1, which is the same as the surface energy shown in Figure 3. This abstracts the quantization phenomenon in an electronic structure and its relationship with the surface energy.

4. Discussion

It is well known that metallic oxides offer great potential for application to catalysts, not only for clean energy applications but also for pollution mitigation. Typically applied dioxides are α-MnO_2 and rutile TiO_2. Their nanometer structure is ideal for attaining the greatest catalytic action. However, there are only a few valid theories that can be used to guide their design. The determination of the intrinsic mechanism of the surface effects and the correlation with the bulk surface or crystal has attracted the attention of many researchers. Deringer and Csányi [16] and Tompsett et al. [17] determined the geometric configuration of α-MnO_2 and rutile TiO_2 nanorods by applying the Wulff construction method, the results of which were corroborated by experiment. Hummer et al. [18] compared the discrepancy between the total calculated nanoparticles surface energies and the summed energies of the constituent faces for rutile TiO_2 and inferred that they uncorrelated with each other as the discrepancy was large. However, they are not able to identify the contributors to the surface effect. In the present study, the surface energies of the α-MnO_2 nanorods exhibit a quantization phenomenon. Following the growth of the nanorods, the surface energies

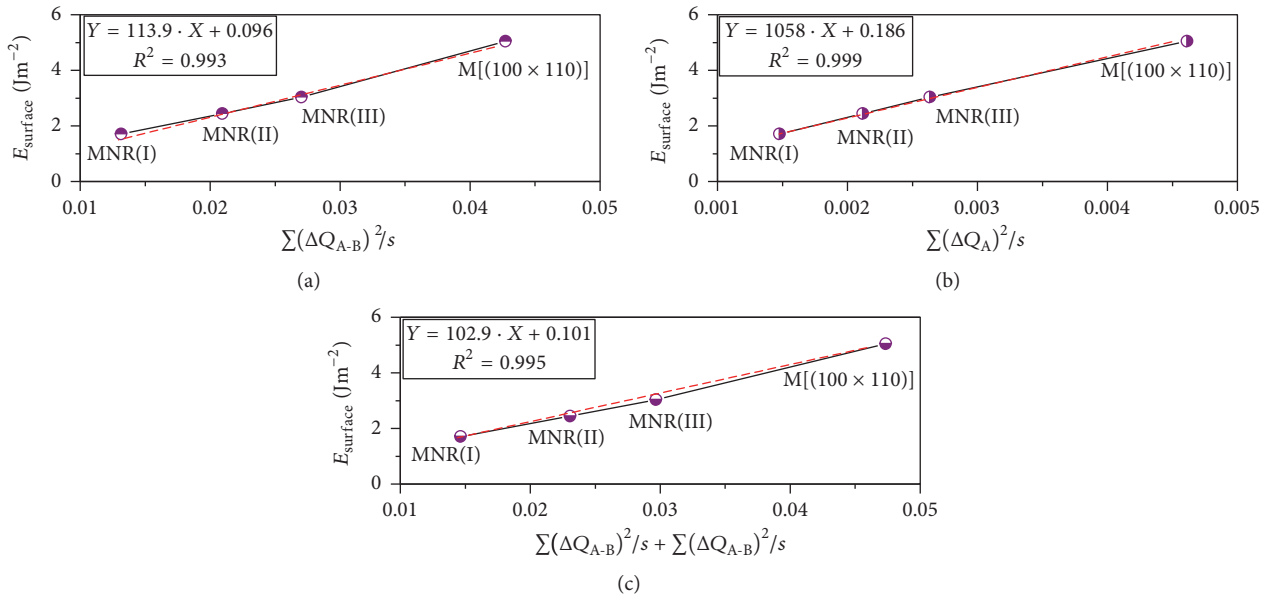

FIGURE 9: Schematic curve of surface energy versus Normalizing Mulliken population or Mulliken charge of α-MnO_2 in different morphologies with nanostructure.

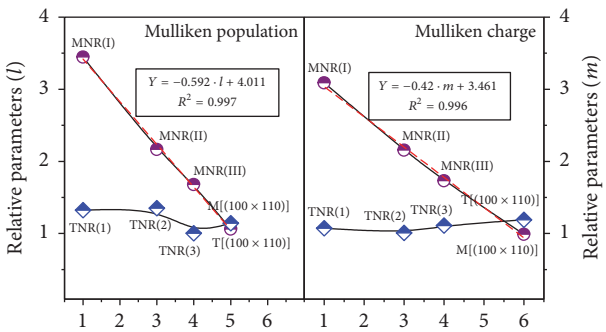

FIGURE 10: Formulized treatment on Mulliken population and Mulliken charge of α-MnO_2 and rutile TiO_2 in different morphologies.

of the nanorods are defined by the function $E_{surface}$ = 1.0401 Jm^{-2} + N×0.608 Jm^{-2}, where N is a positive integer and is a maximum value of 6. Then, considering only the surface energies of the α-MnO_2 nanorods, the optimal structure is identified. Considering their stability, they also obey the following law: $E_{a\text{-}cohesive}/E_{cohesive}$ MNR ≈ 1.09. The interaction between the surface energy and cohesive energy in the quantization phenomenon also conforms to the following commonly held view: the growth of the surface energy of nanometer materials will adversely affect their structural stability. This evolution character of the α-MnO_2 nanorods differs from that of rutile TiO_2. It is found that the surface energies of rutile TiO_2 nanorod and microfacet conform to another function: $E_{surface}$TNR ≈ 1.0102 × 1.1997 Jm^{-2}, which means that the surface energy will remain nearly constant during the growth of rutile TiO_2 nanomaterials. This phenomenon indicates that the surface effect would have a similar impact on a catalyst consisting of rutile TiO_2 nanorods, ignoring their morphologies. Regarding their structural stability, it is found that their cohesive energy conforms to the following rule: $E_{a\text{-}cohesive}/E_{cohesive}$ TNR ≈ 1.00. This phenomenon indicates that the rutile TiO_2 nanorods will exhibit a better structural stability during the manufacturing process, relative to α-MnO_2 nanorods. With further analysis, their quantization phenomenon originates from the evolution character of the electronic structure in terms of the difference in the bond strength and the atomic charge, rather than the geometric configuration. From the previous analysis, the surface energies of α-MnO_2 nanorods and microfacet are increased straightly with the summation of $\sum(\Delta Q_{A\text{-}B})^2/s$ and $\sum(\Delta Q_A)^2/s$, but they keep constant for rutile TiO_2. Mulliken population and charge are originated from the valence electrons of component elements from their formulas [28]. In other words, if we enhance the valence electrons of α-MnO_2 catalysts by doping process, their surface activity would be improved because of the increased surface energy. So it is not hard to understand why their doping elements for MnO_2 catalysts are Pt [29], Pd [29], Ag [30], Nb [31], Fe [32], and so on, which are translation metals with abundance of valence electrons instead of metalloid elements. But for rutile TiO_2 nanorods and microfacet, their surface energies are fluctuating smoothly with the summation of $\sum(\Delta Q_{A\text{-}B})^2/s$ and $\sum(\Delta Q_A)^2/s$. So if we dope the rutile TiO_2 catalysts with translation metals, such as Fe, V, and Cr [33–35], their improved effect would be very limited because the catalytic performance of rutile TiO_2 is sensitive to its change of energy gap [36]. Then the doping processes for rutile TiO_2 catalysts are used for the metalloid elements, such as N [37], Sn [38], and S [39], which affects the internal bonding orbitals. Conclusively limited by their surface energies of rutile TiO_2 nanomaterials, the optimized way to enhance the catalytic performance of rutile TiO_2 is that doping technology appending nanofabrication instead of single nanofabrication method. Then our

investigation has a vital significance to understand and help the optimized processed of metallic oxides catalysts.

Space limitations mean that, within the scope of this paper, we have not been able to address other Miller indexes for α-MnO_2 or rutile TiO_2 nanorods, such as {112}, {211}, and {111} for the α-MnO_2 nanorods and {101} for the rutile TiO_2 nanorods, as mentioned by Deringer and Csányi [16] and Tompsett et al. [17], respectively, although their proportions are smaller than those of the (100) and (110) Miller indexes for α-MnO_2 or rutile TiO_2 nanorods. However, we do not think that this flaw influences the significance of this paper, given that we began by identifying the evolution mechanism of the metallic oxidation of MO_2 (M = Mn, Ti) nanorods and microfacet, which have a correlation with their bulk surfaces and structures. The overall evolution character of metallic oxidation MO_2 (M = Mn, Ti) nanorods and their other nanometer structures will be revealed and addressed in our future research. Furthermore, the evolution mechanism between a nanometer structure and bulk surface will be useful for investigating the intrinsic mechanisms of nanoeffects.

5. Conclusion

The evolution mechanism of metallic dioxide MO_2 (M = Mn, Ti) from nanorods to bulk crystal has been investigated by first-principles calculation. The results of the investigation show the following:

(1) The surface energies of α-MnO_2 and rutile TiO_2 nanorods and microfacets have a quantization phenomenon. For α-MnO_2, it is found that the surface energy conforms to the function: $Y = A + N \times B$, where A is equal to $1.0401\,Jm^{-2}$, B is equal to $0.6648\,Jm^{-2}$, and N is equal to a positive integer of no more than 6. For rutile TiO_2, the surface energy conforms to another function: $E_{surface}$TNR $\approx 1.0102 \times 1.1997\,Jm^{-2}$, which remains constant regardless of the geometric structure of the rutile TiO_2 nanorods.

(2) The cohesive energies of the α-MnO_2 and rutile TiO_2 microfacets and nanorods also have a quantization phenomenon. For α-MnO_2, it is found that the cohesive energy conforms to the function $E_{a\text{-}cohesive}/E_{cohesive}$ MNR ≈ 1.09, where $E_{a\text{-}cohesive}$ is equal to the average of $E_{cohesive}$M(110) and $E_{cohesive}$M(100). For rutile TiO_2, the cohesive energy conforms to $E_{a\text{-}cohesive}/E_{cohesive}$ TNR ≈ 1.00, where $E_{a\text{-}cohesive}$ is equal to the average value of $E_{cohesive}$T(110) and $E_{cohesive}$T(100).

(3) The electronic properties of α-MnO_2 and rutile TiO_2 nanorods and microfacet also exhibit a quantization phenomenon. After being normalized by their surface area, the Mulliken population and Mulliken charge variance of α-MnO_2 exhibit a linear function as $f(n) = 0.5921 * l + 4.011$ for $\sum(\Delta Q_{A\text{-}B})^2/s$ and $f(n) = 0.42 * m + 3.461$. However, the Mulliken population and Mulliken charge variance of rutile TiO_2 exhibit a nearly horizontal line in the evolution from nanorod to microfacet.

Conflicts of Interest

The authors declare that they have no conflicts of interest.

Acknowledgments

This work was supported by the projects of National Natural Science Foundation of China (Grant no. 51361026), Foundation of Jiangxi Educational Committee (GJJ160684), and Key Laboratory of Jiangxi Province for Persistent Pollutants Control and Resources Recycle (Nanchang Hangkong University) (ST201522014).

References

[1] A. El-Sayed, N. Atef, A. H. Hegazy, K. R. Mahmoud, R. M. A. Hameed, and N. K. Allam, "Defect states determined the performance of dopant-free anatase nanocrystals in solar fuel cells," *Solar Energy*, vol. 144, pp. 445–452, 2017.

[2] J. Luo, C. Hu, X. Meng, J. Crittenden, J. Qu, and P. Peng, "Antimony Removal from Aqueous Solution Using Novel α-MnO2 Nanofibers: Equilibrium, Kinetic, and Density Functional Theory Studies," *ACS Sustainable Chemistry & Engineering*, vol. 5, no. 3, pp. 2255–2264, 2017.

[3] Z. Hu, X. Xiao, C. Chen et al., "Al-doped α-MnO2 for high mass-loading pseudocapacitor with excellent cycling stability," *Nano Energy*, vol. 11, pp. 226–234, 2015.

[4] K. B. Liew, W. R. Wan Daud, M. Ghasemi et al., "Manganese oxide/functionalised carbon nanotubes nanocomposite as catalyst for oxygen reduction reaction in microbial fuel cell," *International Journal of Hydrogen Energy*, vol. 40, no. 35, pp. 11625–11632, 2015.

[5] N. K. Allam, K. Shankar, and C. A. Grimes, "A general method for the anodic formation of crystalline metal oxide nanotube arrays without the use of thermal annealing," *Advanced Materials*, vol. 20, no. 20, pp. 3942–3946, 2008.

[6] J. S. Fischel, M. H. Fischel, and D. L. Sparks, "Advances in understanding reactivity of manganese oxides with arsenic and chromium in environmental systems," *ACS Symposium Series*, vol. 1197, pp. 1–27, 2015.

[7] L. Yan, S. Hu, J. Duan, and C. Jing, "Insights from arsenate adsorption on rutile (110): Grazing-incidence X-ray absorption fine structure spectroscopy and DFT+U study," *The Journal of Physical Chemistry A*, vol. 118, no. 26, pp. 4759–4765, 2014.

[8] H.-Y. T. Chen, S. Tosoni, and G. Pacchioni, "A DFT study of the acid–base properties of anatase TiO2 and tetragonal ZrO2 by adsorption of CO and CO2 probe molecules," *Surface Science*, vol. 652, pp. 163–171, 2016.

[9] Y. Xi and J.-C. Ren, "Design of a CO Oxidation Catalyst Based on Two-Dimensional MnO2," *The Journal of Physical Chemistry C*, vol. 120, no. 42, pp. 24302–24306, 2016.

[10] Y. Crespo and N. Seriani, "A lithium peroxide precursor on the α-MnO2 (100) surface," *Journal of Materials Chemistry A*, vol. 2, no. 39, pp. 16538–16546, 2014.

[11] K. Selvakumar, S. M. Senthil Kumar, R. Thangamuthu et al., "Physiochemical investigation of shape-designed MnO2 nanostructures and their influence on oxygen reduction reaction activity in alkaline solution," *The Journal of Physical Chemistry C*, vol. 119, no. 12, pp. 6604–6618, 2015.

[12] N. G. Petrik and G. A. Kimmel, "Photoinduced dissociation of O2 on rutile TiO2(110)," *The Journal of Physical Chemistry Letters*, vol. 1, no. 12, pp. 1758–1762, 2010.

[13] A. S. Barnard, S. Erdin, Y. Lin, P. Zapol, and J. W. Halley, "Modeling the structure and electronic properties of Ti O2 nanoparticles," *Physical Review B: Condensed Matter and Materials Physics*, vol. 73, no. 20, Article ID 205405, 2006.

[14] A. S. Barnard, P. Zapol, and L. A. Curtiss, "Modeling the morphology and phase stability of TiO_2 nanocrystals in water," *Journal of Chemical Theory and Computation*, vol. 1, no. 1, pp. 107–116, 2005.

[15] A. S. Barnard and P. Zapol, "Effects of particle morphology and surface hydrogenation on the phase stability of TiO_2," *Physical Review B: Condensed Matter and Materials Physics*, vol. 70, no. 23, Article ID 235403, 2004.

[16] V. L. Deringer and G. Csányi, "Many-Body Dispersion Correction Effects on Bulk and Surface Properties of Rutile and Anatase TiO2," *The Journal of Physical Chemistry C*, vol. 120, no. 38, pp. 21552–21560, 2016.

[17] D. A. Tompsett, S. C. Parker, and M. S. Islam, "Surface properties of α-MnO2: Relevance to catalytic and supercapacitor behaviour," *Journal of Materials Chemistry A*, vol. 2, no. 37, pp. 15509–15518, 2014.

[18] D. R. Hummer, J. D. Kubicki, P. R. C. Kent, J. E. Post, and P. J. Heaney, "Origin of nanoscale phase stability reversals in titanium oxide polymorphs," *The Journal of Physical Chemistry C*, vol. 113, no. 11, pp. 4240–4245, 2009.

[19] Z. Chen, G. Li, H. Zheng, X. Shu, J. Zou, and P. Peng, "Mechanism of surface effect and selective catalytic performance of MnO2 nanorod: DFT+U study," *Applied Surface Science*, vol. 420, pp. 205–213, 2017.

[20] C. S. Johnson, D. W. Dees, M. F. Mansuetto et al., "Structural and electrochemical studies of α-manganese dioxide (α-MnO2)," *Journal of Power Sources*, vol. 68, no. 2, pp. 570–577, 1997.

[21] J. K. Burdett, T. Hughbanks, G. J. Miller, J. W. Richardson Jr., and J. V. Smith, "Structural-electronic relationships in inorganic solids: Powder neutron diffraction studies of the rutile and anatase polymorphs of titanium dioxide at 15 and 295 K," *Journal of the American Chemical Society*, vol. 109, no. 12, pp. 3639–3646, 1987.

[22] T. Kubo, H. Orita, and H. Nozoye, "Surface structures of rutile TiO2 (011)," *Journal of the American Chemical Society*, vol. 129, no. 34, pp. 10474–10478, 2007.

[23] M. D. Segall, P. J. D. Lindan, M. J. Probert et al., "First-principles simulation: ideas, illustrations and the CASTEP code," *Journal of Physics: Condensed Matter*, vol. 14, no. 11, pp. 2717–2744, 2002.

[24] M. E. Arroyo-De Dompablo, A. Morales-Garca, and M. Taravillo, "DFTU calculations of crystal lattice, electronic structure, and phase stability under pressure of TiO2 polymorphs," *The Journal of Chemical Physics*, vol. 135, no. 5, Article ID 054503, 2011.

[25] T. H. Fisher and J. Almlof, "General methods for geometry and wave function optimization," *The Journal of Physical Chemistry C*, vol. 96, no. 24, pp. 9768–9774, 1992.

[26] M. Ramamoorthy, D. Vanderbilt, and R. D. King-Smith, "First-principles calculations of the energetics of stoichiometric TiO2 surfaces," *Physical Review B: Condensed Matter and Materials Physics*, vol. 49, no. 23, pp. 16721–16727, 1994.

[27] P. J. Lindan, N. M. Harrison, M. J. Gillan, and J. A. White, "First-principles spin-polarized calculations on the reduced and reconstructed," *Physical Review B: Condensed Matter and Materials Physics*, vol. 55, no. 23, pp. 15919–15927, 1997.

[28] M. D. Segall, R. Shah, C. J. Pickard, and M. C. Payne, "Population analysis of plane-wave electronic structure calculations of bulk materials," *Physical Review B: Condensed Matter and Materials Physics*, vol. 54, no. 23, pp. 16317–16320, 1996.

[29] E. Rezaei, J. Soltan, N. Chen, and J. Lin, "Effect of noble metals on activity of MnOx/γ-alumina catalyst in catalytic ozonation of toluene," *Chemical Engineering Journal*, vol. 214, pp. 219–228, 2013.

[30] M. Özacar, A. S. Poyraz, H. C. Genuino, C.-H. Kuo, Y. Meng, and S. L. Suib, "Influence of silver on the catalytic properties of the cryptomelane and Ag-hollandite types manganese oxides OMS-2 in the low-temperature CO oxidation," *Applied Catalysis A: General*, vol. 462-463, pp. 64–74, 2013.

[31] Z. Lian, F. Liu, H. He, X. Shi, J. Mo, and Z. Wu, "Manganese-niobium mixed oxide catalyst for the selective catalytic reduction of NO_x with NH_3 at low temperatures," *Chemical Engineering Journal*, vol. 250, pp. 390–398, 2014.

[32] M. Sun, L. Yu, F. Ye et al., "Transition metal doped cryptomelane-type manganese oxide for low-temperature catalytic combustion of dimethyl ether," *Chemical Engineering Journal*, vol. 220, pp. 320–327, 2013.

[33] K. Nagaveni, M. S. Hegde, and G. Madras, "Structure and photocatalytic activity of $Ti_{1-x}M_xO_{2\pm\delta}$ (M = W, V, Ce, Zr, Fe, and Cu) synthesized by solution combustion method," *The Journal of Physical Chemistry B*, vol. 108, no. 52, pp. 20204–20212, 2004.

[34] H. Yamashita, M. Honda, M. Harada et al., "Preparation of titanium oxide photocatalysts anchored on porous silica glass by a metal ion-implantation method and their photocatalytic reactivities for the degradation of 2-propanol diluted in water," *The Journal of Physical Chemistry B*, vol. 102, no. 52, pp. 10707–10711, 1998.

[35] M. Salmi, N. Tkachenko, R.-J. Lamminmäki, S. Karvinen, V. Vehmanen, and H. Lemmetyinen, "Femtosecond to nanosecond spectroscopy of transition metal-doped TiO2 particles," *Journal of Photochemistry and Photobiology A: Chemistry*, vol. 175, no. 1, pp. 8–14, 2005.

[36] L. Yang, M. Liu, Y. Liu et al., "Theoretical analyses of organic acids assisted surface-catalyzed reduction of CrVI on TiO2 nanowire arrays," *Applied Catalysis B: Environmental*, vol. 198, pp. 508–515, 2016.

[37] A. Kadam, R. Dhabbe, D.-S. Shin, K. Garadkar, and J. Park, "Sunlight driven high photocatalytic activity of Sn doped N-TiO2 nanoparticles synthesized by a microwave assisted method," *Ceramics International*, vol. 43, no. 6, pp. 5164–5172, 2017.

[38] M. Lübke, I. Johnson, N. M. Makwana et al., "High power TiO_2 and high capacity Sn-doped TiO2 nanomaterial anodes for lithium-ion batteries," *Journal of Power Sources*, vol. 294, pp. 94–102, 2015.

[39] K. C. Christoforidis, S. J. A. Figueroa, and M. Fernández-García, "Iron-sulfur codoped TiO 2 anatase nano-materials: UV and sunlight activity for toluene degradation," *Applied Catalysis B: Environmental*, vol. 117-118, pp. 310–316, 2012.